



PCCP

**Thermoelectrics in Ice Slabs: Charge Dynamics and Thermovoltages**

Journal:	<i>Physical Chemistry Chemical Physics</i>
Manuscript ID	CP-ART-05-2021-002304.R1
Article Type:	Paper
Date Submitted by the Author:	27-Jun-2021
Complete List of Authors:	Zhang, Hongwei; Virginia Polytechnic Institute and State University, Mechanical Engineering de Poorter, John; Horatio vzw Mukherjee, Ranit; Virginia Polytechnic Institute and State University, Mechanical Engineering Boreyko, Jonathan; Virginia Tech, USA, Biomedical Engineering & Mechanics Qiao, Rui; Virginia Polytechnic Institute and State University, Mechanical Engineering

SCHOLARONE™  
Manuscripts

# Thermoelectrics in Ice Slabs: Charge Dynamics and Thermovoltages

Hongwei Zhang<sup>a</sup>, John De Poorter<sup>b\*</sup>, Ranit Mukherjee<sup>a</sup>, Jonathan B. Boreyko<sup>a</sup>, and Rui Qiao<sup>a†</sup>

<sup>a</sup> Department of Mechanical Engineering, Virginia Tech, Blacksburg, VA 24061, USA

<sup>b</sup> Horatio vzw, Koningin Maria Hendrikaplein 64d, Ghent 9000, Belgium

June 25, 2021

## Abstract

Thermoelectric effects of ice play an important role in many natural and engineering phenomena. We investigate, numerically and analytically, the electrification of finite-thickness ice slabs due to an imposed temperature difference across them. When exposed to a temperature gradient, thermoelectrification involves a fast initial stage dominated by Bjerrum defects and a subsequent slow stage driven by ionic defects. The time scales of the first and second stages are derived analytically and correspond to the Debye time scales based on the density of Bjerrum and ionic defects, respectively. For a given ice slab, at steady state, the thermovoltage across it and the charge accumulation near its two ends depends strongly on its thickness, with the sensitivity of thermovoltage being more pronounced. The discrepancy between the computed thermovoltage and experimental measurements is analyzed. The analysis shows that, although thermoelectric effects in ice were discovered 50 years ago, significant gaps, ranging from bulk and interfacial properties of defects to measurement of thermovoltage, exist in their quantitative understanding that require further experimental and theoretical/computational studies.

---

\*To whom correspondence should be addressed, email: john.zarat@gmail.com.

†To whom correspondence should be addressed, email: ruiqiao@vt.edu.

## 1 Introduction

In presence of a temperature gradient, an electrical potential difference can develop across an ice sample.<sup>1,2</sup> For example, Latham and Mason discovered that, when a temperature difference was imposed across a 0.5 cm-thick cylindrical ice specimen, a thermovoltage  $V/\Delta T$  of  $\sim -2$  mV/K is developed along the specimen, with the colder end being at a higher potential.<sup>1</sup> The thermoelectrification of ice has been implicated in natural phenomena such as thunderstorm charging,<sup>3-8</sup> and could potentially be exploited in engineering applications including electrostatic de-icing and energy harvesting.<sup>9</sup> The kinetics of thermoelectric voltage and charge development, as well as their magnitude at steady state, often determine the contribution of thermoelectrification in natural phenomena and the effectiveness of harnessing thermoelectric effects in engineering applications. Therefore, there is a need to understand the electrification of ice both from the static and dynamic perspectives.

Fundamentally, the electrification of ice originates from the separation of charge carriers. In undoped, crystalline ice, there are mainly two types of charge carriers due to the formation of defects. The first type of carrier is ionic point defects,  $H^+$  and  $OH^-$  ions, which are formed by the transfer of a proton from one  $H_2O$  molecule to a neighbouring molecule. The second type of carrier is the Bjerrum defects that are generated from the reorientation of water molecules that break the ice rule, with D (L) defects carrying a positive (negative) effective charge.<sup>10</sup> These charge carriers not only determine ice's bulk electrical and optical properties (e.g., conductivity) but also its interfacial properties (e.g., adhesion of ice to metal surfaces and reactivity of ice surfaces).<sup>11-18</sup> The charge separation induced by a temperature gradient in ice is understood conceptually as follows. Because charge carriers are usually formed through thermal activation, a temperature gradient induces a density gradient of these carriers, which in turn leads to their diffusion toward the colder end of the ice. As the diffusivity of different carriers is different, such diffusion would initially cause a net current. This current causes charge accumulation at the cold and warm ends of the ice, which induces an internal electric field (and thus potential difference) across the ice. The induced electric field enhances the transport of slowly diffusing carriers and suppresses the transport of fast diffusing carriers, and eventually reduces the net current across the ice to zero. This process is similar to the generation of a diffusion potential and an ambipolar electric field in electrolytes.<sup>1,19</sup>

The above conceptual picture of thermoelectrification of ice has been formulated into quanti-

tative theories. The first model was proposed by Latham and Mason.<sup>1</sup> Their model considers the diffusion and thermal diffusion of  $H^+$  and  $OH^-$  ions, as well as their migration driven by an electric field. Due to a lack of knowledge of the mobility of Bjerrum defects at that time, the transport of these majority carriers was neglected, although a relative permittivity of 100 was used to account for their contributions to the dielectric screening in ice. Taking the diffusion coefficient ratio of  $D_{OH^-}$  and  $D_{H^+}$  ions as  $D_{OH^-}/D_{H^+} = 0.1$  and the activation energy for the formation of  $H^+$  and  $OH^-$  ions as  $\Phi_{\pm} = 1.2$  eV, their model predicts a thermovoltage that is within 10% of the value measured in their experiments.<sup>1</sup> Shortly after, Jaccard formulated an improved model by explicitly including the transport of majority carriers D and L.<sup>20</sup> The transport of charge carriers formulated by Jaccard includes an extra term associated with the so-called configuration vector, which was recently shown to represent the polarization effects.<sup>21</sup> An analytical formula for the thermovoltage was derived and it can reproduce the experimentally measured thermovoltage of around -2 mV/K reported by Latham and Mason by assuming that  $D_{OH^-}/D_{H_3O^+} \ll 1$ ,<sup>22</sup> and the mobility ratio of L and D defects is  $D_L/D_D \approx 1.2$ .<sup>20</sup> These assumptions, however, do not agree well with the more recent understanding of the transport properties of ionic and Bjerrum defects, e.g., it is now generally thought that  $D_L/D_D \gg 1$ .<sup>10</sup> Since then, few theoretical and modeling studies on the thermoelectrics of ice have been reported.

The pioneering works by Latham, Mason, and Jaccard advanced the fundamental understanding of ice's thermoelectric behavior. Nevertheless, many important issues remain to be understood. First, the spatial distribution and relative magnitude of different charge carriers near the boundaries of a thermally electrified ice slab are poorly known. Second, how the finite thickness of ice affects its thermoelectric characteristics is not clear. These issues were not addressed in prior works because the boundaries of ice were not explicitly considered in them. Third, the transient dynamics of thermoelectrification (e.g., the development of charge separation) and the underlying carrier transport have not been elucidated. Finally, the prediction of the thermovoltage formula developed in those work has not been scrutinized in light of different experimental data on the thermodynamic and transport properties of charge carriers in ice. These fundamental issues are also relevant to practical problems. For example, in response to a temperature gradient, the temporal development of charge and the spatial distribution of different charge carriers near ice boundaries can affect the amount of charge that can be transferred when ice particles of different temperature collide, which may contribute to the charge generation in thunderstorms.<sup>3,6,7</sup> Further, the magnitude of the electrical potential and charge that develop across thin ice sheets or tiny icicles with a characteristic

1 size less than several to a few hundred micrometers can determine what voltage must be applied  
 2 to remove them from their substrates via electrostatic forces.<sup>9</sup>

3 In this work, thermally-induced charge separation in ice slabs of finite thickness is investigated  
 4 both numerically and analytically. In Section 2, the physical and mathematical models for thermo-  
 5 electrification of ice are presented. In Section 3, the evolution of charge carrier distributions in the  
 6 ice slab as well as the charge near each boundary of the ice slab contributed by different carriers  
 7 are presented. The effects of the ice slab thickness on the thermoelectric charge and voltage are  
 8 discussed next. The predictions of thermovoltage by existing analytical theories are then critically  
 9 analyzed in light of our results. Finally, conclusions are drawn in Section 4.

## 10 2 Physical and Mathematical Models

11 We investigate the thermoelectrification of an ice slab that has a thickness of  $W$  in the  $x$ -direction  
 and extends infinitely in the  $yz$ -plane. Before imposing the temperature gradient, 13 equilibrium is  
 assumed throughout the ice slab and thus the ice is electrically neutral everywhere. 14 At  $t = 0$ , a linear  
 temperature profile is imposed across the ice slab in  $x$ -direction, with the temper-15 ature at the left and  
 right ends of the slab set to  $T(x = 0) = T_m + \Delta T/2$  and  $T(x = W) = T_m - \Delta T/2$  16 where  $T_m$  is the  
 temperature at its middle plane ( $x = W/2$ ). We seek to elucidate the development 17 of charge separation  
 and thermoelectric voltage due to the imposed temperature gradient. To this 18 end, the evolution of the  
 densities of charge carriers due to an imposed temperature gradient in the 19 ice must be solved. The  
 evolution of the density of a charge carrier  $i$  is given by

$$\frac{\partial n_i}{\partial t} = -\dot{R}_i + \dot{G}_i - \frac{\partial j_i}{\partial x} \quad (1)$$

20 with  $n_i$  and  $j_i$  the number density and flux of a carrier  $i$ , respectively. The two terms  $\dot{R}_i$  and  $\dot{G}_i$   
 21 refer to the annihilation and generation of defect pairs. Here, we consider four point defects D, L,  
 22  $H^+$ , and  $OH^-$  and they are denoted as  $i = D, L, +$ , and  $-$ , respectively. The term  $\dot{R}_i$  accounts for  
 23 the continuous annihilation of charge carrier  $i$  through recombination with other carriers (i.e., D  
 24 with L or  $H^+$  with  $OH^-$ ). Following the mass action law, the recombination rate is given by

$$\dot{R}_q = \dot{R}_m = \frac{n_+ n_-}{n_+^0 \tau_{\pm}} \quad , \quad \dot{R}_D = \dot{R}_L = \frac{n_D n_L}{n_D^0 \tau_{DL}} \quad (2)$$

1 where  $n_i^0$  is the equilibrium density of carrier  $i$ .  $\tau_{\pm}$  and  $\tau_{DL}$  are the recombination time constants  
 2 for the ionic and Bjerrum pairs, respectively.  $n_i^0$  is given by

$$n_+^0 = n_-^0 = \frac{2}{3}N_o e^{\frac{-\Phi_{\pm}}{2k_B T}} \quad , \quad n_D^0 = n_L^0 = N_o e^{\frac{-\Phi_{DL}}{2k_B T}} \quad (3)$$

3 with  $N_o = 3 \times 10^{28} \text{ m}^{-3}$  the oxygen atom density in ice,<sup>10</sup>  $k_B T$  the thermal energy, and  $\Phi_i$  the  
 4 activation energy of defect  $i$  (note that  $\Phi_+ = \Phi_- = \Phi_{\pm}$ ,  $\Phi_D = \Phi_L = \Phi_{DL}$ ).<sup>10</sup>

5 The term  $\dot{G}_i$  in Equ. (1) accounts for the continuous generation of pairs of D/L and  $\text{H}^+/\text{OH}^-$   
 6 defects through thermal activation. Because the number of  $\text{H}_2\text{O}$  molecule is orders of magnitude  
 7 larger than the number of defects,  $\dot{G}_i$  can be taken as constants given by

$$\dot{G}_+ = \dot{G}_- = \frac{n_+^0 n_-^0}{n_+^0 \tau_{\pm}} \quad , \quad \dot{G}_D = \dot{G}_L = \frac{n_D^0 n_L^0}{n_D^0 \tau_{DL}} \quad (4)$$

8 The flux of the four charge carriers is described by the reinterpreted Jaccard equation:<sup>10,21</sup>

$$j_+ = -D_+ \frac{\partial n_+}{\partial x} + \mu_+ n_+ E + \frac{\mu_+ n_+}{e_{\pm}} \frac{\Phi}{e_{DL}} P_b \quad (5)$$

$$j_- = -D_- \frac{\partial n_-}{\partial x} - \mu_- n_- E - \frac{\mu_- n_-}{e_{\pm}} \frac{\Phi}{e_{DL}} P_b \quad (6)$$

$$j_D = -D_D \frac{\partial n_D}{\partial x} + \mu_D n_D E - \frac{\mu_D n_D}{e_{DL}} \frac{\Phi}{e_{DL}} P_b \quad (7)$$

$$j_L = -D_L \frac{\partial n_L}{\partial x} - \mu_L n_L E + \frac{\mu_L n_L}{e_{DL}} \frac{\Phi}{e_{DL}} P_b \quad (8)$$

12 where subscripts  $+$ ,  $-$ ,  $D$ ,  $L$  denote carrier  $\text{H}^+$ ,  $\text{OH}^-$ , D and L, respectively.  $D_i$  ( $\mu_i$ ) is the diffusion  
 13 coefficient (mobility) of carrier  $i$ .  $D_i$  and  $\mu_i$  are related by  $D_i = \mu_i k_B T_m / |e_i|$ , where  $e_i$  is carrier  
 14  $i$ 's effective charge ( $e_D = -e_L = e_{DL}$  and  $e_+ = -e_- = e_{\pm}$ ), while  $T_m$  is the temperature at the  
 15 middle of the ice slab. Given that the temperature range considered in this work is small,  $D_i$  and  
 16  $\mu_i$  are taken as constant.  $E$  is the electric field and  $P_b$  is the polarization density.  $\Phi$  is a factor  
 17 that relates the change in entropy to the polarization density given by  $\Phi = 8k_B T r_{OO} / \sqrt{3}$ , where  
 18  $r_{OO} = 2.76 \text{ \AA}$  is the distance between two adjacent oxygen atoms in ice.<sup>10,23</sup> As we have recently  
 19 shown, the defect fluxes given by Eqs. (5-8) consist of the classical diffusion (the first flux term)  
 20 and the transport driven by the electrical field and the polarization fields (the second and third  
 21 flux terms).<sup>21</sup>

1 The electric field and polarization density are governed by electrostatic laws

$$-\frac{\partial^2 \phi}{\partial x^2} = \frac{\partial E}{\partial x} = \frac{e_{\pm}(n_+ - n_-) + e_{DL}(n_D - n_L)}{\epsilon_0 \epsilon_{\infty}} \quad (9)$$

2

$$-\frac{\partial^2 \chi}{\partial x^2} = -\frac{\partial P_b}{\partial x} = e_{DL}(n_D - n_L - n_+ + n_-), \quad (10)$$

3 where  $\phi$  is the electric potential and  $P_b = \partial \chi / \partial x$ . In Eq. (9),  $\epsilon_{\infty} = 3.2$  accounts for the electronic 4  
polarization effects of H<sub>2</sub>O molecules in an electric field.<sup>10</sup> Note that while the right-hand side of 5 Eq. (9)  
includes both bound and free charge of all defects, that of Eq. (10) includes only the bound 6 charge of  
defects. As highlighted recently,<sup>21</sup> a D (L) defect has only a bound charge of  $e_{DL} = 0.38e$  ( $-e_{DL} =$   
 $-0.38e$ ), but a H<sup>+</sup> (OH<sup>-</sup>) ion features both a free charge of  $e$  ( $-e$ ) and a bound charge 8 of  $-e_{DL}$  ( $e_{DL}$ ),  
resulting in an effective charge of  $e_{\pm} = 0.62e$  ( $-e_{\pm} = -0.62e$ ).

9 The model given by Eqs. (1 - 10) is closed by the following boundary conditions and initial  
10 conditions:

$$\begin{aligned} j_i|_{x=0} &= 0 \quad , \quad j_i|_{x=W} = 0 \\ \left. \frac{\partial \phi}{\partial x} \right|_{x=0} &= 0 \quad , \quad \phi|_{x=W} = 0 \\ \left. \frac{\partial \chi}{\partial x} \right|_{x=0} &= 0 \quad , \quad \chi|_{x=W} = 0 \end{aligned} \quad (11)$$

11

$$n_i(x)|_{t=0} = N_o e^{\frac{-\Phi_i}{2k_B T(x)}} \quad , \quad \phi|_{t=0} = 0 \quad , \quad \chi|_{t=0} = 0 \quad (12)$$

12 We note that the mathematical model given by Eqs. (1 - 12) neglects surface and interfacial 13 effects  
that can potentially affect the thermoelectrification process. For example, even in the 14 absence of a  
temperature gradient, an ice surface may be charged due to the different affinity of 15 different defects to  
the surface.<sup>24</sup> Further, in the region close to an ice surface, defects can behave 16 differently from that in  
bulk, e.g., D defects can have activation energy smaller than those of L 17 defects, and their mobility is  
larger than that of L defects.<sup>15</sup> These non-bulk effects are not included 18 in our model because the related  
mathematical model and parameters are not yet well established. 19 As we shall see, even with these  
effects neglected, the thermoelectrification exhibits rich physics. 20 Understanding such physics helps lay  
foundation for incorporating the more complicated surface 21 and interfacial physics in future studies of  
thermoelectrification.

### 3 Results and Discussion

We study the thermoelectrification of ice slabs with different thicknesses while keeping the temperature gradient  $\Delta T/W$  at 30 K/m. Without losing generality,  $T_m$  is fixed at 253 K. The thermodynamic and transport properties of the charged defects play a crucial role in determining the thermoelectrification. These properties depend on the way the ice sample was prepared and the reported values vary considerably.<sup>10</sup> Table 1 summarizes the parameters adopted here. Note that the activation energies and mobilities of defects are taken from Table 6.4 of Ref. 10, except that  $\mu_D$  is set to  $1/50 \mu_L$  and  $\Phi_{DL}$  is taken as the median of the range of its plausible values (0.66-0.79 eV). These parameters are within the range of reported data for *bulk* ice in the literature (see Table S1 in the supplementary Information).<sup>10,25</sup> Importantly, these parameters embody three key characteristics of the point defects in ice. First, because  $\Phi_{\pm}$  is 0.65 eV larger than  $\Phi_{DL}$ , the equilibrium density of  $D/L$  pairs at 253 K is  $4.75 \times 10^6$  times higher than that of  $H^+/OH^-$  pairs. This is consistent with the consensus that Bjerrum defects are the majority charge carriers in *bulk* ice, whose density is many orders of magnitude larger than that of ionic defects. Second,  $\mu_+ = 3.33\mu_-$  is consistent with the fact that the  $H^+$  ion is modestly more mobile than  $OH^-$  ions. Third,  $\mu_L = 50\mu_D$  conforms to the generally accepted idea that, in bulk ice, L defects are more mobile than D.<sup>10</sup> The effect of the charge carriers' thermodynamic and transport properties on the thermoelectric voltage at steady state is separately discussed in Section 3.3.

**Table 1:** Properties of defects in ice adopted in the calculations.

Parameter	Value	Ref.	Parameter	Value	Ref.
$\mu_+$	$1 \times 10^{-7} \text{ m}^2/(\text{V}\cdot\text{s})$	10	$\Phi_{DL}$	0.75 eV	-
$\mu_-$	$3 \times 10^{-8} \text{ m}^2/(\text{V}\cdot\text{s})$	10	$\Phi_{\pm}$	1.40 eV	10
$\mu_D$	$4 \times 10^{-10} \text{ m}^2/(\text{V}\cdot\text{s})$	-	$\tau_{DL}$	$2 \times 10^{-5} \text{ s}$	17
$\mu_L$	$2 \times 10^{-8} \text{ m}^2/(\text{V}\cdot\text{s})$	10	$\tau_{\pm}$	$7 \times 10^{-4} \text{ s}$	17

Below we first present the transient dynamics and subsequent steady state of the thermoelectrification of a relatively thick ice slab, and then analyze the dependence of the thermoelectric voltage and charge on the ice thickness. Unless mentioned otherwise, results are presented in dimensionless form: the carrier density, length, and time are non-dimensionalized using the following reference



scales:

$$n_r = n_D^0(T_m) \quad l_r = \lambda_{DL} = \sqrt{\frac{\epsilon_0 \epsilon_\infty k_B T_m}{2e_{DL}^2 n_D^0(T_m)}} \quad t_r = \frac{l_r^2}{D_L} \quad (13)$$

1 where  $n_D^0$  is the equilibrium density of D defects at ice slab's middle plane.  $\lambda_{DL}$  is the Debye length  
 2 defined based on the density of majority carriers (D and L defects) at ice slab's middle plane. An  
 3 intrinsic length scale of ice as an electrolyte is  $\lambda_{DL}$ . Another intrinsic length scale of ice is the Debye  
 4 length associated with the minority carriers ( $H^+$  and  $OH^-$  ions),  $\lambda_\pm = \sqrt{\epsilon_0 \epsilon_\infty k_B T_m / (2e_\pm^2 n_\pm^0(T_m))}$ .  
 5  $t_r$  is the Debye time scale of L defect. At  $T_m = 253$  K, with  $\Phi_{DL}$  and  $\Phi_\pm$  chosen in Table 1,  $\lambda_{DL}$   
 6 and  $\lambda_\pm$  are  $0.12 \mu\text{m}$  and  $0.16 \text{ mm}$ , respectively.  $t_r$  is  $32.2 \mu\text{ s}$ .

### 7 3.1 Thermoelectrification of a finite ice slab

8 We consider the thermoelectrification of a  $0.1 \text{ m}$ -thick ice slab, in which a bulk-like region  
 9 with zero space charge exists around its middle plane. Figure 1a,b show the evolution of the  
 10 thermovoltage across the slab ( $\Delta\phi = \phi(0) - \phi(W)$ ) and the total charge in the slab's left half ( $\sigma_{tot}$ ),  
 11 respectively. The total charge in the slab's right half is opposite to  $\sigma_{tot}$  and thus not shown. We  
 12 observe that, after a temperature gradient is imposed, the ice slab's electrification exhibits two  
 13 distinct stages. In the first, fast stage,  $\Delta\phi$  and  $\sigma_{tot}$  initially increase rapidly and then approach  
 14 their positive pseudo-steady state at  $t \sim 10\lambda_{DL}^2/D_L$  ( $\sim 0.3 \text{ ms}$  with the parameters chosen in Table  
 15 1). This is followed by a second, slow stage, during which both  $\Delta\phi$  and  $\sigma_{tot}$  decrease and approach  
 16 their negative steady state value at  $t \sim 6 \times 10^7 \lambda_{DL}^2/D_L$  ( $\sim 30 \text{ min}$ ).

17 Before analyzing the dynamics of the fast and slow stages of thermoelectrification, it is worth-  
 18 while to compare the computed thermovoltage and charge with the analytical theory by Jaccard.<sup>20</sup>  
 19 He studied the thermoelectric behavior of very thick ice slabs (i.e., boundary effects are neglected) at  
 20 steady state. His theory is built upon the idea that, at steady state,  $e_{DL}(j_D - j_L) + e_\pm(j_+ - j_-) = 0$   
 21 (the total-charge current is zero) and  $e_{DL}(j_D - j_L) - e_{DL}(j_+ - j_-) = 0$  (the bound-charge current  
 22 is zero), which can be combined to arrive at the necessary condition for reaching steady state:

$$j_D - j_L = j_+ - j_- = 0 \quad (14)$$

23 Physically, this condition requires that, at steady state, the currents due to both Bjerrum and ionic  
 24 defects are zero. Using this condition and assuming that  $n_i(x) = n_i^0(T(x))$  ( $i = q, m, D$ , and  $L$ )

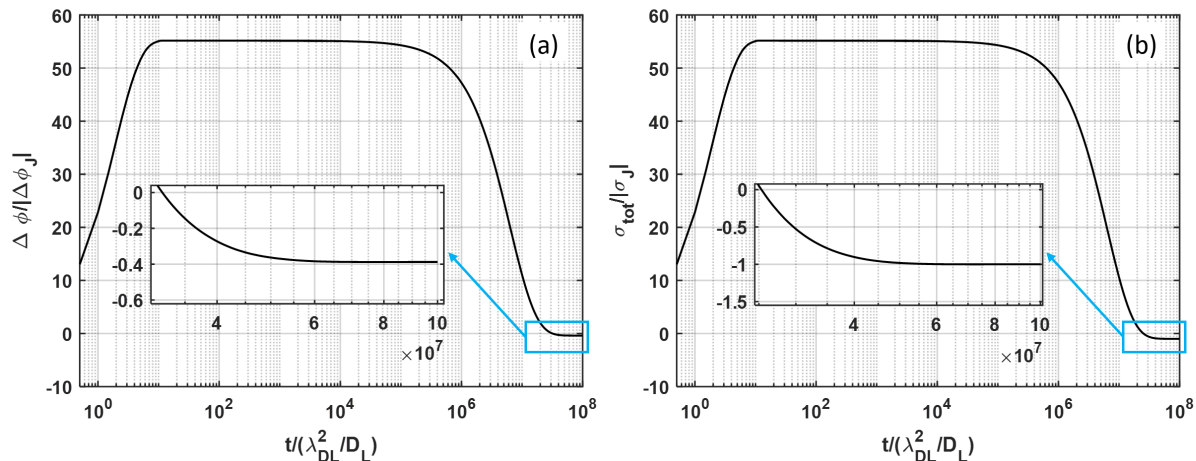


**Figure 1:** (a) Evolution of the thermovoltage across the 0.1 m-thick ice slab. (b) Evolution of the total charge in the left half of the ice slab.

1 and  $\Delta T \ll T_m$ , the steady state thermovoltage for the problem defined in Section 2 is

$$\Delta\phi_J = -\frac{1}{2e} \left[ \frac{1 - \beta_{\pm}}{1 + \beta_{\pm}} \Phi_{\pm} + \frac{1 - \beta_{DL}}{1 + \beta_{DL}} \Phi_{DL} \right] \frac{\Delta T}{T_m} \quad (15)$$

2 where  $\beta_{\pm} = D_-/D_+$  and  $\beta_{DL} = D_L/D_D$ . The total charge in the warmer half of the ice slab is  
 3 given by  $\sigma_J = \epsilon_0 \epsilon_{\infty} \Delta\phi_J / W$ . Examining the values of  $\Delta\Phi$  and  $\sigma_{tot}$  shown in Fig. 1 at large time,  
 4 we observe that the steady state thermovoltage  $\Delta\Phi$  is only  $\sim 40\%$  of that predicted using Eq. 15,  
 5 while  $\sigma_{tot}$  is predicted with an error less than 0.1% by Jaccard's theory. These results highlights  
 6 the importance of finite thickness in affecting thermoelectrification and will be analyzed in Section  
 7 3.2.

8 In the following, we analyze the fast and slow stages of electrification process in detail.

### 9 3.1.1 Fast stage

10 When a temperature gradient is just imposed across on an ice slab, each defect follows its  
 11 quasi-equilibrium density corresponding to the local temperature. The higher density of defects in  
 12 the left (warmer) part of ice thus drives their diffusion toward the right (colder) part of ice. Because  
 13 L defects diffuse faster than D defects, their density near ice slab's left boundary decreases. This  
 14 reduces the annihilation rate of D and L defects there, but does not alter their generation rate (see  
 15 Eq. 2 and 4). Because D defects generated locally diffuse away slowly, their density near the left  
 16 boundary increases. Overall, as shown in Fig. 2a, near the left boundary, D defects are enriched

- 1 but L defects are depleted; the opposite occurs near the right boundary.

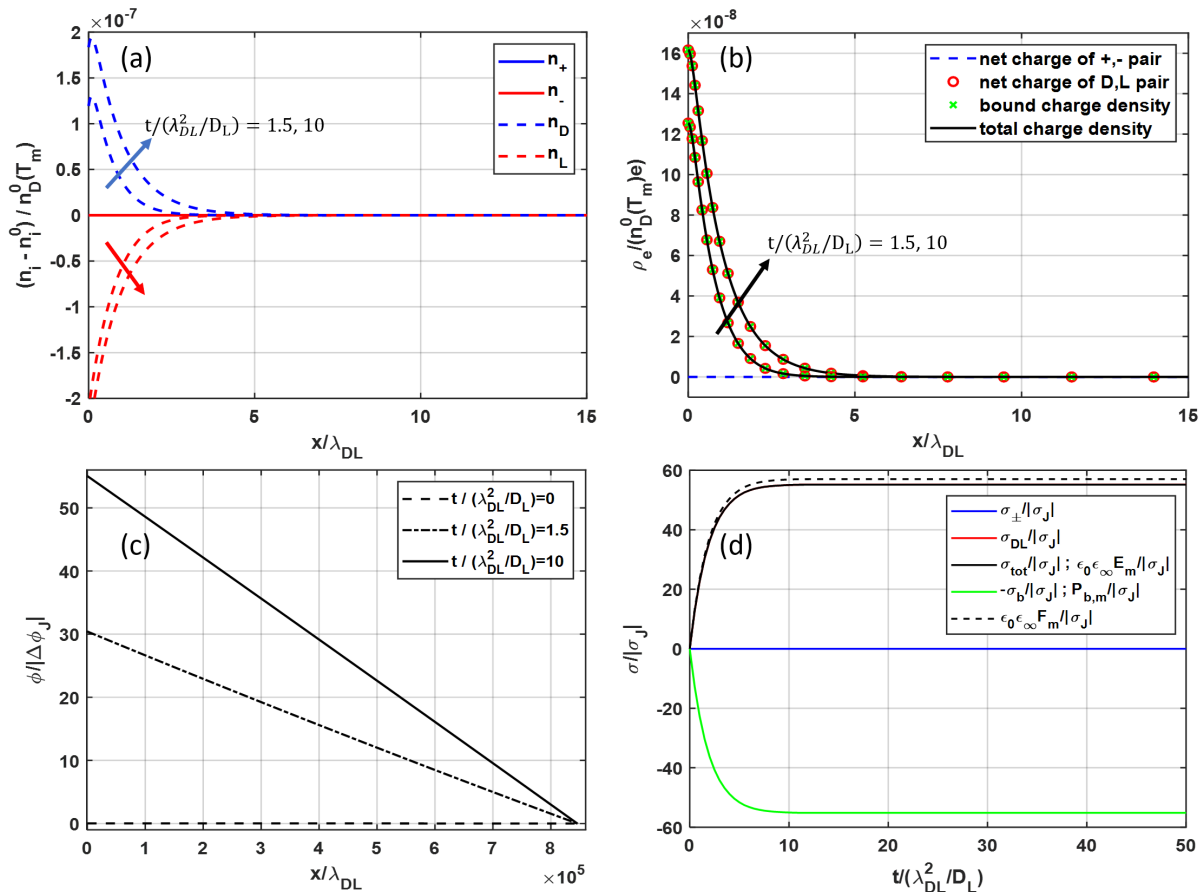


**Figure 2:** Charge dynamics during the fast stage of thermoelectrification in an ice slab. (a) Evolution of ionic and Bjerrum defect density profiles. Note that the density of ionic defects is close to zero and thus their curves overlap. (b) space charge density profile and its components. (c) electric potential profile. (d) Evolution of space charge in ice slab's left half and the electric and polarization fields at ice slab's middle plane. In (a-b), profiles at two time instants are shown near the left boundary (arrows indicate the direction of increasing time). In (d),  $E_m$ ,  $P_{b,m}$ , and  $F_m$  are the electric, polarization, and F-field at ice slab's middle plane.

- 2 The above processes also occur for ionic defects. However, because their density is  $\sim 10^6$  times  
 3 smaller than that of Bjerrum defects, their density change associated with the above processes is  
 4 minuscule compared to that of Bjerrum defects *during the fast stage* (see Fig. 2a). Therefore, we  
 5 focus on density evolution and charge dynamics of Bjerrum defects below, and neglect those of  
 6 ionic defects whenever reasonable.

- 7 The accumulation of D defects and depletion of L defects near the left boundary, together with  
 8 the opposite phenomenon near the right boundary, leads to a charge separation there (see Fig. 2b).

1 Due to negligible contributions of ionic defects, the space charge distribution near these boundaries  
 2 is determined almost solely by the Bjerrum defects that carry bound charges only. Overall, charge  
 3 separation is confined within  $\sim 5\lambda_{DL}$  from each boundary, as expected for charge separation in  
 4 electrolytes.<sup>26</sup> The charge separation leads to an electric potential that decreases from the left to  
 5 the right boundary (see Fig. 2c), mostly in a linear manner because charge separation is limited to  
 6 a narrow zone near each boundary.

7 The development of thermoelectric potential across the ice slab generates an electric field  
 8 pointing toward its right boundary (from the hot to the cold side). This field drives the migration  
 9 of D (L) defects toward the right (left) boundary. As shown in Fig. 2d, such a migration effect  
 10 slows down the accumulation of positive (negative) charge near the right (left) boundary that is  
 11 driven by the diffusion effect. As charge accumulation is enhanced with increasing time, the electric  
 12 field increases proportionally (see Fig. 2d). Eventually, the migration effect becomes strong enough  
 13 to balance the diffusion effect so that no further charge accumulation occurs and a steady state is  
 14 reached. Such a picture on how a steady state is reached, however, is only a partial view of the  
 15 charge dynamics during fast stage. This is because it neglects the buildup of polarization field  $P_b$   
 16 and its effect on the transport of defects, which are useful for understanding why only a pseudo-  
 17 steady state is reached at the end of the fast stage and how a genuine steady state is reached at  
 18 the end of the slow stage.

19 To better appreciate how the pseudo-steady state is reached in the fast stage, it is instructive  
 20 to analyze the transport of D and L defects into/out of ice slab's left half through the slab's middle  
 21 plane. This analysis is facilitated by the fact that, near the middle plane of the rather thick ice  
 22 slab considered here, all defects are at local equilibrium (i.e.,  $n_i(x) = n_i^0(T(x))$ ), which makes the  
 23 evaluation of defect fluxes and their components straightforward.

24 Table 2 summarizes the direction of fluxes of Bjerrum defects through ice slab's middle plane  
 25 (referred to with a subscript  $m$ ) and the associated currents, i.e.,  $i_{DL,m} = e_{DL}(j_{D,m} - j_{L,m})$ .  
 26 The diffusion fluxes of D and L defects are both constant and in positive direction. The faster  
 27 (slower) diffusion of L (D) defects makes the net diffusion current negative. This leads to the  
 28 charge accumulation shown in Fig. 2b and d, which generates an electric field that drives D (L)  
 29 defects toward ice slab's right (left) boundary and thus a positive net migration current. Because  
 30 Bjerrum defects carry only bound charges, their separation near the slab's boundaries generates a  
 31 polarization field  $P_b = -\epsilon_0\epsilon_\infty E$ . This field is opposite to the electric field but drives the transport of  
 32 Bjerrum defects in the same direction as the electric field (see Eq. 7 and 8). Together the electric

1 and polarization fields drive a positive total current, countering the charge accumulation driven  
 2 by the constant diffusion current. Charge accumulation near the ice slab's boundaries eventually  
 3 stops when the migration-polarization current balances the diffusion current, thereby leading to an  
 4 apparent steady state (see Eq. 14).

**Table 2:** Direction of Bjerrum defect fluxes and currents at ice slab's middle plan during the fast stage ( $\rightarrow/\leftarrow$  means toward ice slab' right/left boundary).

	diffusion	electric migration	polarization effect
$j_{D,m}$	$\rightarrow$	$\rightarrow$	$\rightarrow$
$j_{L,m}$	$\rightarrow$	$\leftarrow$	$\leftarrow$
$i_{DL,m}$	$\leftarrow$	$\rightarrow$	$\rightarrow$

5 Building upon the above analysis, both the time scale and the asymptotic total charge near  
 6 each boundary of the fast stage can be obtained analytically. Using Eq. 7-8 and taking advantage  
 7 of the fact that the region near the ice slab's middle plane is bulk-like, (i.e.,  $n_D(x) = n_L(x) =$   
 8  $n_D^0(T(x)) = n_{DL}^0(T(x))$  near  $x = W/2$  and  $n_D|_{x=W/2} = n_L|_{x=W/2} = n_{DL,m}^0$ ), the net excess of D  
 9 defects over L defects in ice slab's left half follows

$$\frac{d(\Gamma_D - \Gamma_L)}{dt} = j_{L,m} - j_{D,m} = (D_D - D_L) \frac{dn_{DL}^0}{dx} \Big|_{x=W/2} - (D_D + D_L) \frac{e_{DL}}{k_B T_m} n_{DL,m}^0 F \Big|_{x=W/2} \quad (16)$$

10

$$F = E - \frac{\Phi}{e_{DL}^2} P_b \quad (17)$$

11 where  $\Gamma_i = \int_0^{W/2} n_i dx$  is amount of defect  $i$  in ice slab's left half ( $i = D, L$ ).  $F$  is a field representing  
 12 the combined electric-polarization fields driving the transport of charged defects. During the fast  
 13 stage, electric and polarization fields are generated predominately by Bjerrum defects that feature  
 14 only bound charge. Therefore,  $F = (1 + \alpha)E$ , with  $\alpha = \Phi \epsilon_0 \epsilon_\infty / e_{DL}^2 = 0.034$ .  $F|_{x=W/2}$  and  $E|_{x=W/2}$   
 15 are hereafter denoted as  $F_m$  and  $E_m$ , respectively. Integrating Eq. 9 and 10 over the ice slab's left  
 16 half, we have

$$\Gamma_D - \Gamma_L = \frac{\epsilon_0 \epsilon_\infty}{e_{DL}} E_m = \frac{\epsilon_0 \epsilon_\infty}{(1 + \alpha) e_{DL}} F_m \quad (18)$$

17 Substituting Eq. 18 into Eq. 16, we obtain

$$\frac{\epsilon_0 \epsilon_\infty}{(1 + \alpha) e_{DL}} \frac{dF_m(t)}{dt} = -(D_D + D_L) \frac{e_{DL}}{k_B T_m} n_{DL,m}^0 F_m(t) + (D_D - D_L) \frac{dn_{DL}^0}{dx} \Big|_{x=W/2} \quad (19)$$

1 With the initial condition  $F_m(0) = 0$ , the solution of Eq. (19) is

$$F_m(t) = -\frac{q}{p}e^{-pt} + \frac{q}{p} \quad (20)$$

$$p = \frac{n_{DL,m}^0 e_{DL}^2 (1 + \alpha)(D_D + D_L)}{k_B T_m \epsilon_0 \epsilon_\infty} \quad \text{and} \quad q = \frac{dn_{DL}^0}{dx} \frac{e_{DL} (1 + \alpha)(D_D - D_L)}{\epsilon_0 \epsilon_\infty}$$

2 The time scale for  $F_m(t)$  to reach a steady state is thus

$$\tau_{F,f} = \frac{1}{p} = \frac{2\lambda_{DL}^2}{(1 + \alpha)(D_D + D_L)} = 1.9t_r \quad (21)$$

3 Here, with the parameters shown in Table 1,  $\tau_{F,f} = 61.2 \mu\text{s}$ . Physically,  $\tau_{F,f}$  resembles the Debye  
4 time of bulk electrolytes<sup>26</sup> and it is the time scale for development of  $F$  field that drives electric-  
5 polarization transport of Bjerrum defects to balance their current driven by diffusion. Since  $F_m =$   
6  $(1 + \alpha)E_m = (1 + \alpha)\sigma_{tot}/\epsilon_0\epsilon_\infty$ ,  $\tau_{F,f}$  is also the time constant for the development of electric field  
7 and total charge in ice slab. Eq. 19 and 21 thus predict that, at  $3\tau_{F,f} = 5.7t_r$ , the total charge  
8 in ice slab's left half reaches 95% of its plateau value of the fast stage, in agreement with that  
9 observed in Fig. 2d with an error of  $\sim 1\%$ .

10 Using Eq. 3 and 19, at the end of fast stage, the asymptotic value of electric field at ice slab's  
11 middle plane is obtained as

$$E_{m,f} = -\frac{\Phi_{DL}}{2(1 + \alpha)e_{DL}} \left( \frac{1 - \beta_{DL}}{1 + \beta_{DL}} \right) \frac{1}{T_m} \frac{\Delta T}{W} \quad (22)$$

12 The asymptotic value predicted by Eq. 22 for the present problem agrees with that shown in Fig.  
13 2d with an error less than 0.1%.

14 If Bjerrum defects were the only charge carrier, then a genuine steady state would be reached  
15 at the end of processes illustrated above. However, in presence of ionic defects, a genuine steady  
16 state is not reached when  $\sigma_{tot}$  approaches an apparent plateau (see Fig. 2d). Specifically, reaching  
17 a genuine steady state requires the current of ionic defects at ice slab's middle plane associated  
18 with the fluxes of  $\text{H}^+$  and  $\text{OH}^-$  ( $j_{+,m}$  and  $j_{-,m}$ ) to be zero, i.e.,  $i_{\pm,m} = e_{\pm}(j_{+,m} - j_{-,m})$ . Table 3  
19 summarizes the direction of fluxes of ionic defects through ice slab's middle plane and the associated

20 current  $i_{\pm,m}$  during the fast stage of thermoelectrification. The diffusion current associated with  $\text{H}^+$   
21 and  $\text{OH}^-$  ions is positive because  $\text{H}^+$  ions are more mobile. Because the electric field set up by the  
22 separation of Bjerrum defects during the fast stage is positive, the migration currents of ionic defects  
23 is also positive. Because  $\text{H}^+$  ( $\text{OH}^-$ ) ions carry a negative (positive) bound charge, their polarization

1 current is negative. However, because  $P_b = -\epsilon_0\epsilon_\infty E$  during the fast stage as explained above, the  
 2 polarization current of ionic defects is only  $\alpha = 3.4\%$  of their electric migration current (see Eq. 5  
 3 and 6). Hence, the polarization current of ionic defects cannot balance their diffusion and electric  
 4 migration currents. The plateau in Fig. 2d thus represents only a pseudo-steady state. A genuine  
 5 steady state can only be achieved when the current driven by a greatly enhanced polarization field  
 6 balances the current driven by diffusion and electric fields. To enhance the polarization field set  
 7 up by charge separation associated with majority Bjerrum defects, significant charge separation  
 8 contributed by minority ionic defects is needed. However, because of the very low density of ionic  
 9 defects (and thus their current), a significant enhancement of the polarization field can only occur  
 10 at a large time scale, which corresponds to the slow stage of thermoelectrification observed in Fig.  
 11 1.

**Table 3:** Direction of ionic defect fluxes and currents at ice slab’s middle plane during the fast stage and the early part of the slow stage ( $\rightarrow/\leftarrow$  means toward ice slab’ right/left boundary).

	diffusion	electric migration	polarization effects
$\dot{j}_{+,m}$	$\rightarrow$	$\rightarrow$	$\leftarrow$
$\dot{j}_{-,m}$	$\rightarrow$	$\leftarrow$	$\rightarrow$
$i_{\pm,m}$	$\rightarrow$	$\rightarrow$	$\leftarrow$

### 12 3.1.2 Slow stage

13 As pointed out above, after a pseudo-steady state is reached, ionic defects have not yet reached  
 14 their steady state. Their transport is the driving force for thermoelectrification during the sub-  
 15 sequent slow stage. Their transport changes fields built by Bjerrum defects earlier and leads to  
 16 the evolution of the density of Bjerrum and ionic defects, space charge distribution, and potential  
 17 profile shown in Fig. 3a-c. Initially, driven by the electric and polarization fields set up by the  
 18 transport of Bjerrum defects,  $\text{OH}^-$  ( $\text{H}^+$ ) ions are enriched (depleted) near the left boundary, while  
 19 the opposite occurs near the right boundary (see Fig. 3a). As shown in Fig. 3b, near the left  
 20 boundary, this makes the total space charge more negative but the bound charge more positive.  
 21 The latter is due to the fact that the bound charge of an ionic defect is opposite to its effective  
 22 charge.<sup>21</sup> These changes of the total and bound charge distribution weaken the electric field across  
 23 the ice slab (e.g., the slope of electric potential in Fig. 3c) but enhance the polarization field.

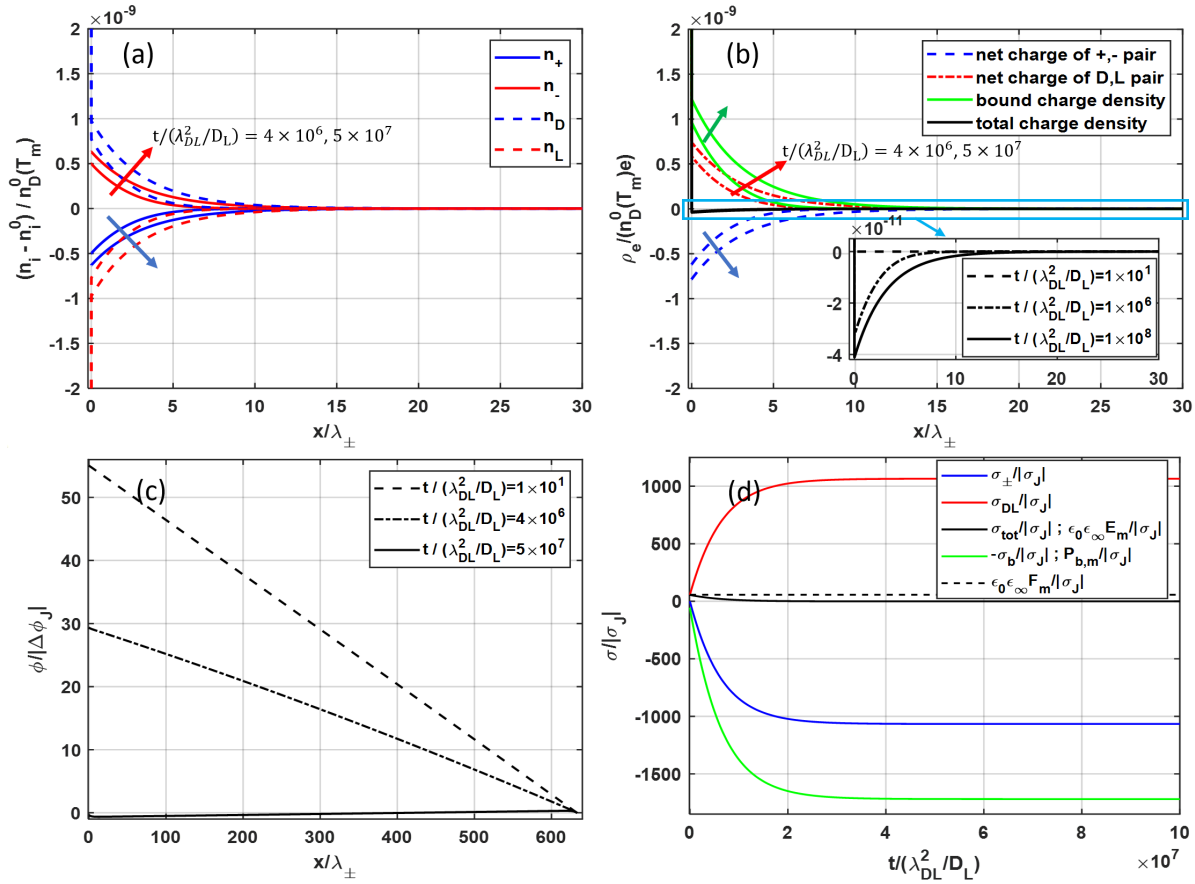


**Figure 3:** Charge dynamics during the slow stage of thermoelectrification. (a-c) Evolution of ionic and Bjerrum defect density profiles (a), space charge density profile and its components (b), and electric potential profile (c) in an ice slab. (d) Evolution of space charge in ice slab's left half and the electric and polarization fields at ice slab's middle plane. In (a-b), profiles at two time instants are shown near the left boundary (arrows indicate the direction of increasing time).

1 The aforementioned transport of ionic defects thus tends to weaken the  $F^-$ -field (refer to Eq.  
 2 17) established through the balance of the diffusion and electric-polarization transport of Bjerrum  
 3 defects. However, this weakening effect is countered easily by the currents generated by the diffusion  
 4 of Bjerrum defects due to their vastly higher density compared to ionic defects. As a result, the  
 5 change of  $F^-$ -field is less than 0.1% (see Fig. 3d) and the accumulation (depletion) of  $\text{OH}^-$  ( $\text{H}^+$ )  
 6 ions near the left boundary is accompanied by the accumulation (depletion) of D (L) defects there  
 7 as can be observed in Fig. 3a. The continued accumulation (depletion) of  $\text{OH}^-$  ( $\text{H}^+$ ) ions near  
 8 ice slab's left boundary eventually brings the sign of net charge from positive at the pseudo-steady  
 9 state to negative and enhances the bound charge there. These changes reduce the electric field to  
 10 negative and strengthen the polarization field greatly at the middle plane, both helping to counter



1 the current generated by diffusion of ionic defects. Eventually, the combined electric-polarization  
2 currents of ionic defects balance their positive diffusion current and a steady state is finally reached.

3 Overall, the thermoelectrification of an ice slab during the slow stage shows two key features.  
4 First, the  $F$ -field varies little because it is controlled primarily by the constant-rate diffusion of  
5 Bjerrum defects; electric and polarization fields change significantly from their values at the fast  
6 stage so that the ionic current they generate eventually balances the diffusion current of ionic  
7 defects. In particular, at the ice slab's middle plane, we have  $\mathcal{O}(dF_m/dt) \ll \mathcal{O}(dE_m/dt)$ , which is  
8 indeed observed in Fig. 3d. Second, the change in the charge of ionic defects near each boundary  
9 is accompanied by a similar change of the net charge of Bjerrum defects. In particular, we have  
10  $\mathcal{O}(d(\Gamma_+ - \Gamma_-)/dt) \sim \mathcal{O}(d(\Gamma_D - \Gamma_L)/dt)$ , which is indeed observed in Fig. 3a and d. Both features  
11 can also be understood by analyzing the transport equations of ionic and Bjerrum defects in a  
12 temperature gradient (see supplementary Information for details).

13 Building upon the insights from the above results, the net charges of ionic and Bjerrum defect  
14 pairs near each boundary and the time scale of the slow stage can be obtained analytically. To  
15 obtain the charge of the two defect pairs near the left boundary ( $\sigma_{\pm} = e_{\pm}(\Gamma_+ - \Gamma_-)$  and  $\sigma_{DL} =$   
16  $e_{DL}(\Gamma_D - \Gamma_L)$ ), we integrate Eq. 9 and 10 over ice slab's left half, apply the boundary conditions  
17 in Eq. 11, and after some algebra, we obtain

$$\sigma_{\pm} = e_{\pm}(\Gamma_+ - \Gamma_-) = P_{b,m} \frac{e_{\pm}}{e} + E_m \epsilon_0 \epsilon_{\infty} \frac{e_{\pm}}{e} \quad (23)$$

18

$$\sigma_{DL} = e_{DL}(\Gamma_D - \Gamma_L) = -P_{b,m} \frac{e_{\pm}}{e} + E_m \epsilon_0 \epsilon_{\infty} \frac{e_{DL}}{e} \quad (24)$$

19 Next, similar to Eq. 16, applying the conservation law for  $H^+$  and  $OH^-$  ions and using Eq. 5, 6,  
20 and 17, the excess of  $H^+$  ions over  $OH^-$  ions in ice slab's left half is obtained as

$$\frac{d(\Gamma_+ - \Gamma_-)}{dt} = -\frac{e}{k_B T_m} n_{\pm,m}^0 (D_+ + D_-) E_m + \frac{e_{DL}}{k_B T_m} n_{\pm,m}^0 (D_+ + D_-) F_m + (D_+ - D_-) \frac{dn_{\pm}^0}{dx} \Big|_{x=W/2} \quad (25)$$

21 where  $n_{\pm,m}^0 = n_+^0(x = W/2) = n_-^0(x = W/2)$ .  $n_{\pm}^0$  is the equilibrium density of ionic defects, which  
22 depends on the local temperature through Eq. 3. Combining Eq. 25 with Eq. 3 and 16, we obtain

$$\frac{\frac{d(\Gamma_+ - \Gamma_-)}{dt}}{(D_+ + D_-) \frac{n_{\pm,m}^0}{k_B T_m}} + \frac{\frac{e}{e_{DL}} \frac{d(\Gamma_D - \Gamma_L)}{dt}}{(D_D + D_L) \frac{n_{DL,m}^0}{k_B T_m}} = -e E_m + \frac{1}{2T_m} \left[ \frac{1 - \beta_{DL}}{1 + \beta_{DL}} \Phi_{DL} + \frac{1 - \beta_{\pm}}{1 + \beta_{\pm}} \Phi_{\pm} \right] \frac{dT}{dx} \quad (26)$$

23 Because  $n_{DL,m}^0 \sim 10^6 n_{\pm,m}^0$  and  $\mathcal{O}(d(\Gamma_+ - \Gamma_-)/dt) \sim \mathcal{O}(d(\Gamma_D - \Gamma_L)/dt)$ , the second term on the

1 left-hand side of Eq. 26 can be neglected. Substituting Eq. 17 and 23 into Eq. 26, we have

$$\frac{d}{dt} \left[ \frac{1}{e} \left( \epsilon_0 \epsilon_\infty E_m + \frac{e^2_{DL}}{\Phi} (E_m - F_m) \right) \right] = -\frac{eE_m}{k_B T_m} + \frac{1}{2k_B T_m^2} \left[ \frac{1 - \beta_{DL}}{1 + \beta_{DL}} \Phi_{DL} + \frac{1 - \beta_{\pm}}{1 + \beta_{\pm}} \Phi_{\pm} \right] \frac{dT}{dx} \quad (27)$$

2 Because  $\mathcal{O}(\partial F_m / \partial t) \ll \mathcal{O}(\partial E_m / \partial t)$ , the  $F_m$  term in Eq. 27 can be neglected to result in

$$\frac{\epsilon_0 \epsilon_\infty + \frac{e^2_{DL}}{\Phi}}{e(D_+ + D_-)n_{\pm,m}^0} \frac{dE_m}{dt} = -\frac{eE_m}{k_B T_m} + \frac{1}{2k_B T_m^2} \left[ \frac{1 - \beta_{DL}}{1 + \beta_{DL}} \Phi_{DL} + \frac{1 - \beta_{\pm}}{1 + \beta_{\pm}} \Phi_{\pm} \right] \frac{dT}{dx} \quad (28)$$

3 Because the slow stage lasts much longer than the fast stage, the initial condition for Eq. 28 can be  
4 approximated as the pseudo-steady state value of  $E_m$  during the fast stage, i.e.,  $E_m(t = 0) = E_{m,f}$ .

5 Therefore, we have

$$E_m(t) = (E_{m,f} - E_m(t = \infty))e^{-t/\tau_{E,s}} + E_m(\infty) \quad (29)$$

6 The steady state electric field at ice slab's middle plane is

$$E_m(t = \infty) = -\frac{1}{2eT_m} \left[ \frac{1 - \beta_{\pm}}{1 + \beta_{\pm}} \Phi_{\pm} + \frac{1 - \beta_{DL}}{1 + \beta_{DL}} \Phi_{DL} \right] \frac{\Delta T}{W} \quad (30)$$

7 The steady state value predicted by Eq. 30 agrees with that shown in Fig. 3d with an error less  
8 than 0.1%. The time scale for  $E_m(t)$  to reach the steady state is

$$\tau_{E,s} = \frac{k_B T_m \left( \epsilon_0 \epsilon_\infty + \frac{e^2_{DL}}{\Phi} \right)}{e^2 (D_+ + D_-) n_{\pm}^0} = \left( 1 + \frac{1}{\alpha} \right) \frac{e_{\pm}^2}{e^2} \frac{\lambda_{\pm}^2}{(D_+ + D_-)/2} \quad (31)$$

9 Substituting the parameters in Table 1,  $\tau_{E,s} = 3.47$  min. Physically,  $\tau_{E,s}$  is similar to the  
10 Debye time of ionic defects and it is the time scale for the development of  $E_m$  and  $P_{b,m}$  fields that  
11 drives electric-polarization transport of ionic defects to balance their current driven by diffusion.  
12 Eq. 29 and 31 predict that, at  $3\tau_{E,s} = 1.94 \times 10^7 t_r$ , the decrease of total charge in ice slab's left  
13 half reaches 95% of the that at steady state, in agreement with the observation in Fig. 3d with an  
14 error less than 1%.

15 Using a similar approach, the steady state value of the polarization field at ice slab's middle  
16 plane,  $P_{b,m}(t = \infty)$ , can be obtained (see supplementary Information). Using the steady state  
17 values of  $P_{b,m}$  and  $E_m$ , the ratio of the net charge of ionic defects near the left boundary ( $\sigma_{\pm}$ ) to

1 the total charge of all defects ( $\sigma_{tot} = \sigma_{\pm} + \sigma_{DL}$ ) can be obtained as

$$\frac{\sigma_{\pm}(t = \infty)}{\sigma_{tot}(t = \infty)} = \frac{e_{\pm}e_{DL}}{e\epsilon_0\epsilon_{\infty}\Phi} \frac{\left[ \frac{1-\beta_{\pm}}{1+\beta_{\pm}}\Phi_{\pm}e_{DL} - \frac{1-\beta_{DL}}{1+\beta_{DL}}\Phi_{DL}e_{\pm} \right]}{\left[ \frac{1-\beta_{\pm}}{1+\beta_{\pm}}\Phi_{\pm} + \frac{1-\beta_{DL}}{1+\beta_{DL}}\Phi_{DL} \right]} + \frac{e_{\pm}}{e} \quad (32)$$

2 Eq. 32 predicts that  $\sigma_{\pm}(t = \infty)/\sigma_{tot}(t = \infty) = 1.07 \times 10^3$ , which agrees with the data shown in  
3 Fig. 3d with an error less than 0.1%.

### 4 3.2 Effect of ice slab thickness on electrification

5 We showed earlier that the steady state thermovoltage across a 0.1 m-thick ice slab obtained  
6 from our numerical simulation is only  $\sim 40\%$  of that predicted by Eq. 15, which was derived by  
7 neglecting boundary effects (or equivalently, assuming that the ice slab is very thick). In this  
8 section, we examine the origin of this significant discrepancy and evaluate the effect of ice slab  
9 thickness on thermoelectrification.

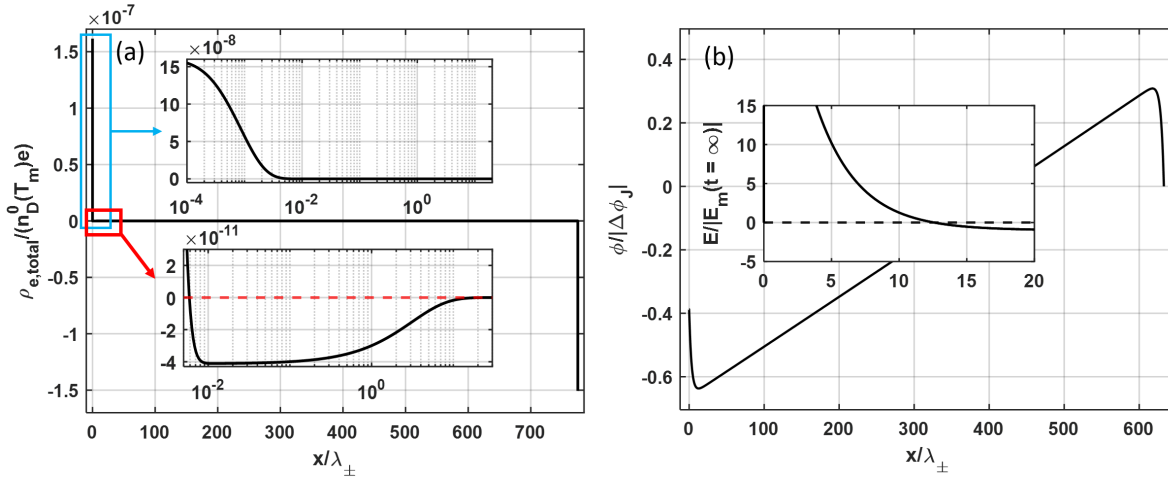


**Figure 4:** Space charge density (a) and electric potential (b) profiles across a 0.1 m-thick ice slab at steady state ( $T(0) - T(W) = 3K$ ). The inset in (b) is the electric field near the left boundary and it is non-dimensionalized using the field given by Eq. 30.

10 Figure 4a shows the distribution of space charge in the ice slab, with zoom-in views near its left  
11 boundary (i.e.,  $x = 0$ ). We observe that the charge distribution features two layers with different  
12 length scales: a compact inner layer and a diffuse outer layer that extend  $\sim 5\lambda_{DL}$  ( $0.59 \mu\text{m}$ ) and  
13  $\sim 15\lambda_{\pm}$  ( $2.37 \text{ mm}$ ) from the left boundary, respectively. The inner layer features positive charge  
14 and is dominated by Bjerrum defects (see Fig. 2b); the outer layer features negative charge and is  
15 contributed more by ionic defects (see Fig. 3b). Because the inner layer is highly charged and the

1 outer layer is much more diffuse than the inner layer, the inner layer's charge is fully screened by the  
 2 counter-charges in the outer layer only at  $x \sim 13\lambda_{\pm}$  (this is evident in the inset of Fig. 4b, where the  
 3 electric field  $E$  becomes zero at  $x/\lambda_{\pm} \sim 13$ ). Therefore, as we move away from the left boundary,  
 4 the electric potential decreases initially. A similar phenomenon occurs near the right boundary.  
 5 Because these interfacial potential variations are significant and opposite to the potential variation  
 6 in bulk ice, they make the overall potential difference across the ice slab considerably smaller than  
 7 that expected from Eq. 15, where the boundary effects are neglected.

8 Interfacial potential drops occur in the boundary regions, whose width is governed by  $\lambda_{\pm}$  and  
 9 is independent of ice slab's thickness. As shown in Fig. 5a, boundary effects play an increasingly  
 10 important role in the overall potential variation across ice slabs when they becomes thinner. Figure  
 11 5b shows that, as  $W/\lambda_{\pm}$  decreases to 316 corresponding to  $W = 5$  cm, the interfacial potential  
 12 drop even causes the thermovoltage across ice slab to reverse sign. As  $W/\lambda_{\pm}$  decreases further to  
 13 19, thermovoltage increases to 1.26 mV/K, with the warmer end at a higher potential.

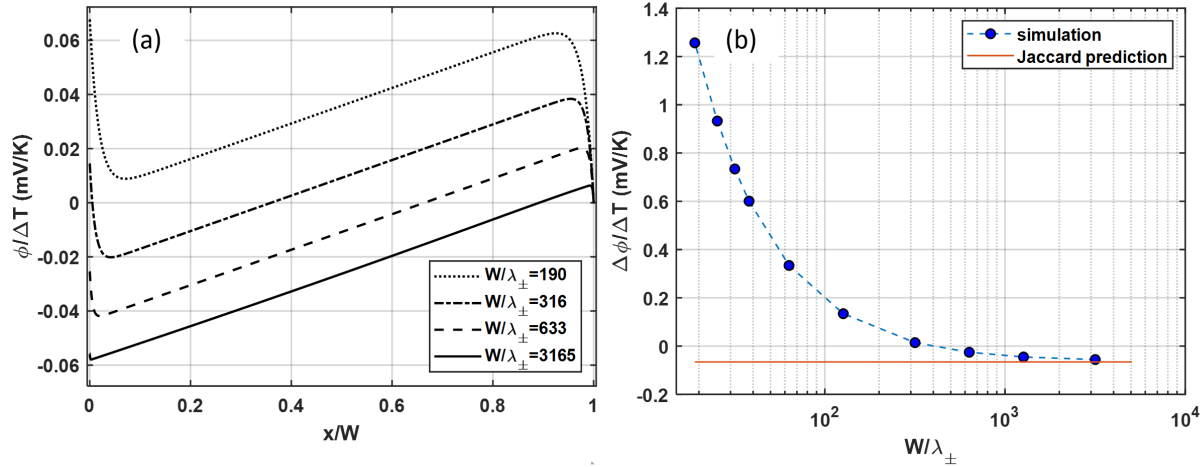


**Figure 5:** (a) Steady state electric potential profiles across ice slabs with different thickness. (b) Variation of the thermoelectric power  $\Delta\phi/\Delta T$  as a function of an ice slab's thickness.  $\Delta\phi/\Delta T > 0$  corresponds to a higher potential at the warmer end of an ice slab.  $\Delta T/W = (T(0) - T(W))/W$  is kept as 30 K/m in all cases.

14 Figure 6a shows the variation of the total charge in the ice slab's left half ( $\sigma_{tot}$ ) as a function of  
 15 its thickness. As the slab thickness decreases,  $\sigma_{tot}$  deviates from that predicted by Eq. 30. To see  
 16 the origins of this deviation, we examine the distribution of Bjerrum and ionic defects in an ice slab  
 17 with  $W = 19\lambda_{\pm}$ . Figure 6b shows the non-equilibrium density of all defects ( $n_i - n_i^0$ ) while Fig. 6c  
 18 shows the density ( $n_i$ ) of the ionic defects across the ice slab. At the ice slab's middle plane, the

1 density of each defect remains close to its local equilibrium (panel b); however, the gradients of ionic  
 2 defects' density deviates from those corresponding to the local equilibrium condition considerably  
 3 (panel c) due to the overlap of the space charge layers. The prediction of the steady state electric  
 4 field at middle plane by Eq. 30 is based on two assumptions (a)  $n_i(x = W/2) = n_i^0(T_m)$  and (b)  
 5  $n_i(x) = n_i^0(x)$  near  $x = W/2$ . However, this second assumption no longer holds for ionic defects  
 6 (see Fig. 6c),  $\sigma_{tot}$  cannot be predicted by Eq. 30 accurately.

7 The dependence of  $\sigma_{tot}$  on slab thickness is weaker compared to that of the thermovoltage.  
 8 Indeed, at  $W > 60\lambda_{\pm}$ ,  $\sigma_{tot}$  already becomes independent of slab thickness and is predicted well  
 9 by Eq. 30. This is expected: unlike thermovoltage that is determined by the potential profile in  
 10 the *entire* ice slab,  $\sigma_{tot}$  is governed by the electric field at ice slab's middle plane, which depends  
 11 much less sensitively on the slab thickness (e.g., in Fig. 5a, the slope of the potential in the middle  
 12 portion of the ice slab barely varies with ice slab thickness while the total potential drop across  
 13 the ice slab is heavily affected by the potential drop near both boundaries). Given the thickness  
 14 dependence of  $\sigma_{tot}$  and the thermovoltage, the choice of sample thickness in experiment deserves  
 15 more attention.

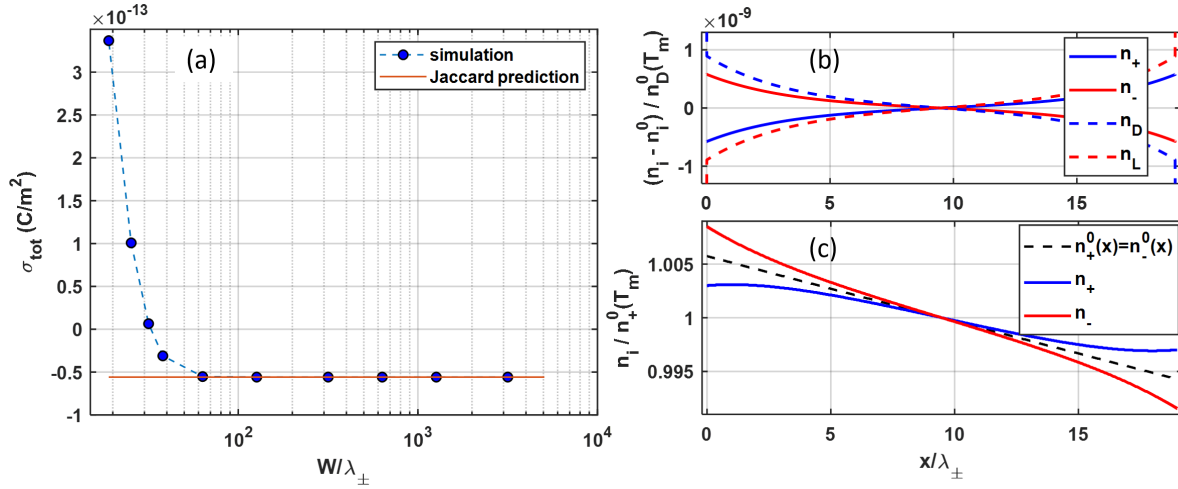


**Figure 6:** (a) Variation of the total charge in an ice slab's left half as a function of its thickness. (b-c) Non-equilibrium density of ionic and Bjerrum defects (b) and density of ionic defects (c) across an ice slab with  $W/\lambda_{\pm} = 19$ .  $(T(0) - T(W))/W = 30 \text{ K/m}$  in all cases.

### 16 3.3 Steady-state thermovoltage

17 The thermoelectric power computed in Section 3.1.2 is  $\Delta\phi/\Delta T = -0.026 \text{ mV/K}$ , which devi-  
 18 ates greatly from the around  $-2 \text{ mV/K}$  measured by Latham and Mason<sup>1</sup> ( $\Delta\phi/\Delta T > 0$  corresponds

1 to higher potential at ice slab's warmer end). Many factors can contribute to this discrepancy.

2 From the theory and modeling perspective, the discrepancy may be attributed to at least  
 3 three reasons. First, the thermodynamic and transport properties of Bjerrum and ionic defects  
 4 used in our models may not be accurate for the ice samples used experimentally. For thick ice  
 5 slabs, their thermoelectric power is described using Eq. 15 and thus depends on four parameters:  
 6 the activation energy of ionic and Bjerrum defects ( $\Phi_{\pm}$  and  $\Phi_{DL}$ ) and the mobility ratio of each  
 7 defect pair ( $\beta_{\pm}$  and  $\beta_{DL}$ ). These properties, however, are not fully understood and rather different  
 8 values have been reported (see Table S1 in the supplementary Information). Of these properties,  
 9  $\Phi_{DL}$  is relatively well established (0.66 to 0.79 eV) and  $\Phi_{\pm}$  is likely 1 to 1.4 eV.  $\beta_{\pm}$  is likely in the  
 10 range of 0.1-0.3, while  $\beta_{DL}$  is thought to be far larger than 1.0.<sup>10</sup> Figure 7 shows that the  $\Delta\phi/\Delta T$   
 11 predicted using Eq. 15 in a plausible parameter space of these properties (note that  $\beta_{DL}$  is varied  
 12 from 1 to 10 because thermovoltage varies little as  $\beta_{DL}$  increases beyond 10. We observe that a  
 13  $\Delta\phi/\Delta T$  in the range of -2.0 to 0.1 mV/K is possible, and the experimentally measured  $\Delta\phi/\Delta T$   
 14 can indeed be captured by the model for some parameter combinations.

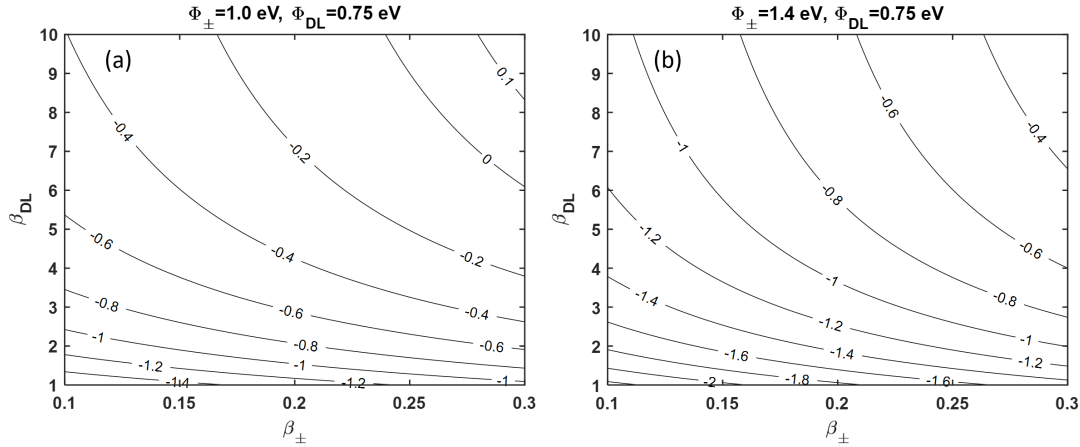


**Figure 7:** The thermoelectric power  $\Delta\phi/\Delta T$  (mV/K) computed using Eq. 15 for different  $\Phi_{\pm}$ ,  $\Phi_{DL}$ ,  $\beta_{\pm}$ , and  $\beta_{DL}$ .  $\Delta\phi/\Delta T > 0$  corresponds to a higher potential at the warmer end of an ice slab.

15 Second, the boundary effects associated with finite thickness of ice slab illustrated in Section  
 16 3.2 can greatly change  $\Delta\phi/\Delta T$ , even reversing its sign. The precise impact of boundary effects on  
 17 the above discrepancy is, however, difficult to quantify. While the thickness of ice slab was usually  
 18 reported in experimental studies, the value of  $W/\lambda_{\pm}$  is difficult to determine because of the large  
 19 uncertainty of the activation energy of ionic defects and thus  $\lambda_{\pm}$ .

1 Third, not all physics governing the thermoelectric behavior of ice have been considered in  
 2 the model adopted here. As an example, the temperature dependence of charge carriers' diffusion  
 3 coefficient (or mobility) is neglected in our model. This effect can be considered by introducing  
 4  $d \ln D_i / dT = \Phi_{D_i} / k_B T^2$ , where  $\Phi_{D_i}$  is the migration energy of a carrier  $i$ .<sup>20</sup> With this modification,  
 5 the thermovoltage given by Eq. 15 must be modified to become<sup>20</sup>

$$\Delta\phi_J = -\frac{1}{e} \left[ \frac{(\Phi_{D_D} + \frac{1}{2}\Phi_{D_L}) - \beta_{DL}(\Phi_{D_L} + \frac{1}{2}\Phi_{D_L})}{1 + \beta_{DL}} + \frac{(\Phi_{D_+} + \frac{1}{2}\Phi_{\pm}) - \beta_{\pm}(\Phi_{D_-} + \frac{1}{2}\Phi_{\pm})}{1 + \beta_{\pm}} \right] \frac{\Delta T}{T_m} \quad (33)$$

6 From Eq. 33, we see the migration energy and activation energy affect the thermovoltage in  
 7 qualitatively similar way. The migration energies of ionic and Bjerrum defects (especially those of  
 8 D and OH<sup>-</sup> defects) are less well understood compared to their activation energies. The migration  
 9 energy of the Bjerrum defects is thought to be around 0.2 eV. The migration energy of ionic defects  
 10 is often considered as 0, although negative migration energies arising from tunneling mechanisms  
 11 have also been proposed (see Table S1 in the supplementary Information).<sup>27</sup>

12 As another example, the model adopted here neglects physics that cause defects near interfaces  
 13 to exhibit behavior different from that in bulk ice. In reality, defects near ice surface may behave  
 14 differently from that in bulk ice, e.g., they may have mobilities and activation energies different  
 15 from those in bulk.<sup>15</sup> Some of these neglected physics can affect the separation of defect pairs  
 16 near ice surfaces and consequently the thermoelectric behavior of ice, thereby explaining to the  
 17 discrepancy between experimental data and prediction by the present thermoelectric model.

18 From the experimental perspective, the measured thermoelectric behavior may depend on the  
 19 nature of ice samples used, which can depend on how samples were prepared. Furthermore, the  
 20 measured thermovoltage may not be strictly a property of the ice if the contact potential between  
 21 the ice and electrode itself depends on temperature.

## 22 4 Conclusions

23 In summary, the electrification of ice slabs under a temperature gradient is investigated both  
 24 numerically and analytically. First, we study the dynamics of electrification of a relatively thick  
 25 ice slab after a temperature gradient is imposed. The thermoelectrification occurs in two stages.  
 26 The initial fast stage is dominated by Bjerrum defects, who are the majority charge carriers in ice.  
 27 Charge separation in this stage is confined within  $5\lambda_{DL}$  from the slab boundaries. In the subsequent

1 slow stage, the transport of ionic defects modifies the electric field set up by Bjerrum defects during  
2 the fast stage, while the combined electric and polarization field (the  $F$ -field) changes little. The  
3 charge separation in this stage is confined within  $15\lambda_{\pm}$  from the slab boundaries. The time scales  
4 of the first and second stages are found to correspond to the Debye time scales of Bjerrum and  
5 ionic defects, respectively. The analytical predictions of the total charge near the warm/cold end of  
6 the ice slab and its contributions by Bjerrum and ionic defects independently at the pseudo-steady  
7 state (i.e., the end of the first stage) and at the true steady state are obtained.

8 Next, by imposing a constant temperature gradient across the ice slab, we simulated the ther-  
9 moelectrification of ice slabs with different thickness. The steady-state thermovoltage and charge  
10 accumulation near each boundary are found to depend on ice slab's thickness with the thermovolt-  
11 age displaying a higher sensitivity. Finally, we analyze the discrepancies of thermovoltages predicted  
12 by simulations and measured experimentally. The uncertainties of ice properties, finite thickness  
13 effects, incompleteness of thermoelectric theory, and uncertainties in experimental measurements  
14 are identified as main reasons behind these discrepancies.

15 Thermoelectric effects in ice were discovered experimentally half a century ago, and the theo-  
16 retical studies of these effects culminated in Jaccard's model shortly after.<sup>20</sup> Since then, little work  
17 has been devoted to them and it is often implicitly assumed that these effects are well understood.  
18 The present study, however, suggests that there exist significant gaps in our understanding of these  
19 effects. Given that these effects potentially play an important role in both natural phenomena (e.g.,  
20 lightning in thunderstorms) and can be leveraged for engineering applications (e.g., electrostatic  
21 deicing<sup>9</sup>), we hope this present study will stimulate both experimental and theoretical studies of  
22 these effects in the future.

## 23 Acknowledgments

24 The authors at Virginia Tech acknowledge the NSF for support under grant number 2034242  
25 and thank the ARC office for generous allocation of computer time.

## 26 Supplementary Information

27 The supplementary information include (I) mathematical justification of  $\mathcal{O}(d(\Gamma_+ - \Gamma_-)/dt) \sim$   
28  $\mathcal{O}(d(\Gamma_D - \Gamma_L)/dt)$  and  $\mathcal{O}(dF_m/dt) \ll \mathcal{O}(dE_m/dt)$  during the slow stage of electrification, (II)  
29 derivation of  $P_m$  in the slow stage, and (III) summary of literature value for the properties of the



1 Bjerrum and ionic defects in ice.

## 2 References

- 3 (1) Latham, J.; Mason, B. J. Electric charge transfer associated with temperature gradients in  
4 ice. *Proceedings of the Royal Society of London. Series A. Mathematical and Physical Sciences*  
5 **1961**, *260*, 523–536.
- 6 (2) Takahashi, T. Thermoelectric effect in ice. *Journal of Atmospheric Sciences* **1966**, *23*, 74–77.
- 7 (3) Latham, J.; Stow, C. The influence of impact velocity and ice specimen geometry on the  
8 charge transfer associated with temperature gradients in ice. *Quarterly Journal of the Royal*  
9 *Meteorological Society* **1965**, *91*, 462–470.
- 10 (4) Latham, J.; Miller, A. The role of ice specimen geometry and impact velocity in the Reynolds-  
11 Brook theory of thunderstorm electrification. *Journal of the Atmospheric Sciences* **1965**, *22*,  
12 505–508.
- 13 (5) Takahashi, T. Riming electrification as a charge generation mechanism in thunderstorms.  
14 *Journal of the Atmospheric Sciences* **1978**, *35*, 1536–1548.
- 15 (6) Gaskell, W.; Illingworth, A. Charge transfer accompanying individual collisions between ice  
16 particles and its role in thunderstorm electrification. *Quarterly Journal of the Royal Meteorolo-*  
17 *gical Society* **1980**, *106*, 841–854.
- 18 (7) Jayaratne, E. Temperature gradients in ice as a charge generation process in thunderstorms.  
19 *Atmospheric research* **1993**, *29*, 247–259.
- 20 (8) Nelson, J.; Baker, M. Charging of ice-vapor interfaces: applications to thunderstorms. *Atmo-*  
21 *spheric Chemistry and Physics* **2003**, *3*, 1237–1252.
- 22 (9) Mukherjee, R.; Ahmadi, S. F.; Zhang, H.; Qiao, R.; Boreyko, J. B. Electrostatic Jumping of  
23 Frost. *ACS nano* **2021**, *15*, 4669–4677.
- 24 (10) Petrenko, V.; Whitworth, R. *Physics of Ice*. Oxford Univ. 2002.
- 25 (11) Bilgram, J.; Gränicher, H. Defect equilibria and conduction mechanisms in ice. *Physics of*  
26 *condensed matter* **1974**, *18*, 275–291.

- 1 (12) Collier, W. B.; Ritzhaupt, G.; Devlin, J. P. Spectroscopically evaluated rates and energies for  
2 proton transfer and Bjerrum defect migration in cubic ice. *The Journal of Physical Chemistry*  
3 **1984**, *88*, 363–368.
- 4 (13) Ryzhkin, I. A.; Petrenko, V. F. Physical Mechanisms Responsible for Ice Adhesion. *The Jour-*  
5 *nal of Physical Chemistry B* **1997**, *101*, 6267–6270.
- 6 (14) Uras-Aytemiz, N.; Joyce, C.; Devlin, J. P. Protonic and Bjerrum defect activity near the  
7 surface of ice at  $T_i$  145 K. *The Journal of Chemical Physics* **2001**, *115*, 9835–9842.
- 8 (15) Watkins, M.; VandeVondele, J.; Slater, B. Point defects at the ice (0001) surface. *Proceedings*  
9 *of the National Academy of Sciences* **2010**, *107*, 12429–12434.
- 10 (16) Devlin, J. P. Relating the current science of ion-defect behavior in ice to a plausible mecha-  
11 nism for directional charge transfer during ice particle collisions. *Physical Chemistry Chemical*  
12 *Physics* **2011**, *13*, 19707–19713.
- 13 (17) Shavlov, A.; Dzhumandzhi, V.; Yakovenko, A. Charge of water droplets during evaporation  
14 and condensation. *Journal of Aerosol Science* **2018**, *123*, 17–26.
- 15 (18) Fortes, A. Structural manifestation of partial proton ordering and defect mobility in ice Ih.  
16 *Physical Chemistry Chemical Physics* **2019**, *21*, 8264–8274.
- 17 (19) Prieve, D.; Anderson, J.; Ebel, J.; Lowell, M. Motion of a particle generated by chemical  
18 gradients. Part 2. Electrolytes. *J. Fluid Mech* **1984**, *148*, 247–269.
- 19 (20) Jaccard, C. Thermoelectric effects in ice crystals. *Physik der kondensierten Materie* **1963**, *1*,  
20 143–151.
- 21 (21) De Poorter, J. An improved formulation of Jaccard’s theory of the electric properties of ice.  
22 *The European Physical Journal B* **2019**, *92*, 157.
- 23 (22) Eigen, M.; De Maeyer, L. Self-dissociation and protonic charge transport in water and. *Pro-*  
24 *ceedings of the Royal Society of London. Series A. Mathematical and Physical Sciences* **1958**,  
25 *247*, 505–533.
- 26 (23) Ryzhkin, I. A.; Whitworth, R. W. The configurational entropy in the Jaccard theory of the  
27 electrical properties of ice. *Journal of Physics: Condensed Matter* **1997**, *9*, 395–402.

- 1 (24) Petrenko, V. F.; Ryzhkin, I. A. Surface states of charge carriers and electrical properties of  
2 the surface layer of ice. *The Journal of Physical Chemistry B* **1997**, *101*, 6285–6289.
- 3 (25) Eisenberg, D.; Kauzmann, W.; Kauzmann, W. *The structure and properties of water*; Oxford  
4 University Press on Demand, 2005.
- 5 (26) Bazant, M. Z.; Thornton, K.; Ajdari, A. Diffuse-charge dynamics in electrochemical systems.  
6 *Phys. Rev. E* **2004**, *70*, 021506.
- 7 (27) Kunst, M.; Warman, J. M. Nanosecond time-resolved conductivity studies of pulse-ionized  
8 ice. 2. The mobility and trapping of protons. *The Journal of Physical Chemistry* **1983**, *87*,  
9 4093–4095.